Water Research 200 (2021) 117258

Contents lists available at ScienceDirect

Water Research

journal homepage: www.elsevier.com/locate/watres

Water-level fluctuations regulate the availability and diffusion kinetics process of phosphorus at lake water–sediment interface

Hezhong Yuan[a,*], Haixiang Wang[a], Yanwen Zhou[b], Bingchan Jia[a], Jianghua Yu[a], Yiwei Cai[a], Zhen Yang[c], Enfeng Liu[d], Qiang Li[e], Hongbin Yin[c,*]

[a] Jiangsu Key Laboratory of Atmospheric Environment Monitoring and Pollution Control and Collaborative Innovation Center of Atmospheric Environment and Equipment Technology (CICAEET), School of Environmental Science and Engineering, Nanjing University of Information Science and Technology, Nanjing 210044, China
[b] Nanjing Research Institute of Ecological and Environmental Sciences, Nanjing 210013, China
[c] State Key Laboratory of Lake Science and Environment, Nanjing Institute of Geography and Limnology, Chinese Academy of Sciences, Nanjing 210008, China
[d] College of Geography and Environment, Shandong Normal University, Ji'nan 250359, China
[e] Department of Soil Science, University of Wisconsin-Madison, 53706 Madison, Wisconsin, USA

ARTICLE INFO

Article history:
Received 18 March 2021
Revised 11 May 2021
Accepted 12 May 2021
Available online 18 May 2021

Keywords:
High–resolution evidence
Regulation effect
Phosphorus
Water–sediment interface
Water level fluctuation
Lake

ABSTRACT

Sequential extraction and *in-situ* diffusive gradients in thin films (DGT) techniques were used to determine phosphorus (P) fractions and high-resolution 2D fluxes of labile P_{DGT}, $Fe^{2+}{}_{DGT}$, and $S^{2-}{}_{DGT}$ in sediment systems. The diffusion fluxes were subsequently calculated for different scenarios. Dynamic diffusion parameters between solid sediment and solution were also fitted using the DIFS (DGT-induced fluxes in sediments) model. The results suggested that Fe-bound P (Fe-P) was the dominant pool which contributed to the resupply potential of P in the water–sediment continuum. Significant upward decreases of labile P_{DGT}, $Fe^{2+}{}_{DGT}$, and $S^{2-}{}_{DGT}$ fluxes were detected in pristine and incubated microcosms. This dominance indicated the more obvious immobilization of labile P via oxidation of both Fe^{2+} and S^{2-} in oxidic conditions. Additionally, these labile analytes in the microcosms obviously decreased after a 30-day incubation period, indicating that water-level fluctuations can significantly regulate adsorption–desorption processes of the P bound to Fe-containing minerals within a short time. Higher concentrations of labile P_{DGT}, $Fe^{2+}{}_{DGT}$, and $S^{2-}{}_{DGT}$ were measured at the shallow lake region where more drastic water-level variation occurred. This demonstrates that frequent adsorption–desorption of phosphate from the sediment particles to the aqueous solution can result in looser binding on the solid sediment surface and easier desorption in aerobic conditions via the regulation of water levels. Higher R values fitted with DIFS model suggested that more significant desorption and replenishment effect of labile P to the aqueous solution would occur in lake regions with more dramatic water-level variations. Finally, a significant positive correlation between $S^{2-}{}_{DGT}$ and $Fe^{2+}{}_{DGT}$ in the sediment indicated that the S^{2-} oxidization under the conditions of low water-level can trigger the reduction of Fe(III) and subsequent release of active P. In general, speaking, frequent water-level fluctuations in the lake over time facilitated the formation and retention of the Fe(II) phase in the sediment, and desorption of Fe coupled P into the aqueous solution when the water level was high.

1. Introduction

Eutrophication induced by extensive nutrients inputs in aquatic ecosystems arises more and more frequently and attracts attention worldwide (Mooney et al., 2020). Phosphorus (P) is considered to be crucial in the deterioration of water quality, adjustment of ecosystem functions, and harmful algal blooms in lacustrine ecosystems (Carpenter, 2008). Large amounts of P-containing water and agricultural fertilizer are discharged into the lakes via tributary rivers and terrigenous runoff, which further facilitates phytoplankton growth (Quinlan et al., 2021). The dynamics of P in lake ecosystems are dominantly regulated by the balance between sources and sinks. Change in environmental conditions can release endogenous source of P in the sediment back into the overlying

* Corresponding authors.
E-mail addresses: yuanhezhong@nuist.edu.cn (H. Yuan), hbyin@niglas.ac.cn (H. Yin).

https://doi.org/10.1016/j.watres.2021.117258
0043-1354/

water column (Shinohara et al., 2012). This process is comparable to the exogenous discharge, and potentially fuels primary production in lacustrine ecosystems. Traditional analytical methods based on total concentrations can give useful information about the P transfer processes between the water and sediment. Additionally, sequential chemical extractions using various extractants can differentiate the P phase bound to different metallic (hydrogen)oxides and organic matter (OM) in the sediment (Kim et al., 2003). The varying forms of sequestered P in the sediment can substantially affect their potential for remobilization and resupply in the lakes. However, visual assessments of the dynamic processes of P between water and sediment are scarce. Accurate understanding of the occurrence and diagenesis features of P in the sediment and the interactions of P between the water and the solid sediment is important for the management of P sources and the recovery of eutrophic lakes.

The boundary layer near the sediment is a crucial site in connection with external and internal exchanges of P in lacustrine ecosystems (Riber and Wetzel, 1987). The water–sediment interface often features steep physical and chemical gradients such as dissolved oxygen (DO), pH, redox potential (Eh), and dissolved ions (PO_4^{3+}, Fe^{2+}, S^{2-}, etc.) within narrow distances (Xu et al., 2012). The oxidized microzones in bottom sediments of Lakes Okeechobee and Apopka, USA, vary in depth from a few mm to about 2 cm (Olila and Reddy, 1997). Dissolved oxygen (DO) is one of the predominant controlling factors of P cycling in aquatic environments (Cesbron et al., 2014). Dynamic processes of P, including transformations in speciation and mobility, that occur at the sediment surface are regulated by DO penetration depth of the water–sediment continuum (Simpson et al., 2019). The concentration and dynamic effects of soluble reactive phosphorus (SRP) in the water–sediment continuum are predominantly influenced by the balance between adsorption and desorption to P-containing minerals (Chen et al., 2018). Labile P in the solid sediment can be released into the interstitial water from the binding sites of solid sedimentary particles and consequently upwardly diffuse into overlying water, as seen in increased concentration gradients near the boundary layer, which further fuels the eutrophication in lakes (Ding et al., 2015). These redox-mediated processes in the thin oxidized microzone underlain by a large-scale reduced layer of surficial sediment dominate the remobilization and resupply of P in water.

Hydrological characteristics such as water level can alter the aeration of bottom waters and surficial sediment and further influence the P dynamics in aquatic ecosystems which are susceptible to meteorological conditions, morphology, and exogenous discharge (Vollenweider, 1975). Water quality is influenced by water-level fluctuations in aquatic systems (Wang et al., 2020). For example, seasonal fluctuations between high water level and low water level can result in active changes in energy and matter, including the forms and distribution of P (Mooney et al., 2020; Wang et al., 2020). The observation performed by Qin et al. (2020) suggested that water depth plays a critical role in lake eutrophication and P limitation especially in deep lakes. The seasonal resuspension and settling of particulates depending on water–level fluctuation can determine the Eh status at the water–sediment interface, and subsequently affect the uptake and release of P, especially in Fe-rich systems (Olila and Reddy, 1997). Water–level fluctuations mitigate eutrophication status in some lakes/reservoirs due to the alternation of redox conditions, and has been the focus of attention worldwide (Bao et al., 2015; Gao et al., 2020). However, previous research focused mainly on *ex-situ* measurements of P-containing compounds that can induce the change of physical and chemical characteristics. The study of dynamic processes of P in water–sediment systems during water–sediment fluctuations in lakes is limited due to the lack of high-resolution *in-situ* testing technologies.

In aquatic environment, ferric iron (Fe^{3+}) and sulfate (SO_4^{2-}) as terminal electron acceptors can be simultaneously reduced by heterotrophic bacteria and anaerobic episodes (Azzoni et al., 2001). The integration of P with Fe oxy(hydr)oxides is critical for the immobilization of the labile P fraction in sediment (Norgbey et al., 2020). The reductive dissolution of P bound to Fe-containing minerals in the sediment particles in anoxic conditions plays a key role in releasing P into interstitial water and its subsequent diffusion into overlying water (Cosmidis et al., 2014). Additionally, the reduction of SO_4^{2-} to S^{2-} can influence P bound to Fe-containing minerals, which can stimulate PO_4^{3-} and Fe cycling and eutrophication in lakes (Zhao et al., 2019). To explore the lability and occurrence of P, Fe^{2+}, and S^{2-} in the sediment, previous work has principally focused on *ex-situ* chemical extraction methods (Egger et al., 2016; Chen et al., 2018). Simultaneous *in-situ* detection of these chemical components at high resolution is required to reveal the distribution and dynamic behaviors of these contaminants due to the spatial heterogeneity in the sediment.

Advanced and maneuverable high-resolution techniques are pivotal for the exact exploration of the dynamics of Fe-P-S across the water–sediment interface of lakes. Diffusive gradients in thin films (DGT) is a technique for the *in-situ* visual assessment of the resupply potential of labile analytes such as metal ions, PO_4^{3-}, Fe^{2+}, and S^{2-} from solid phase to aqueous phase (Alexa et al., 2009). As an *in-situ* dynamic speciation technique, a DGT unit consists of diffusive boundary layer, diffusive gel, and binding gel layer (Ding et al., 2018). DGT can enable high-resolution two-dimensional (2D) images of analytes and can supply visual heterogeneity in sediment microstructures at a small or even microscale (Han et al., 2017). A steady-state linear concentration gradient of labile forms of analytes is established between the binding gel and the solution, and maintains the flux of the solute controlled by diffusion (Harper et al., 2000). The DGT-measured fractions are composed of both solute from interstitial water and the further resupply of the solid sediment. As a comparative evaluation of measurements, the diffusion processes of DGT simulate the interaction of labile analytes between solid and solution in the sediment and reflect the actual dynamic behaviors in natural environments (Price et al., 2013). Double-sided DGT techniques combined with traditional analysis methods are used for the synchronous detection of heterogeneous changes of labile P, Fe^{2+}, and S^{2-} in the water–sediment continuum in a representative lake undergoing intense water–level fluctuation over time. The main objectives of this study are to: 1) characterize *in-situ* 2D flux changes of labile P, Fe^{2+}, and S^{2-} using a novel high-resolution DGT technique in the water–sediment continuum that experiences the change of water depth; 2) elaborate the resupply mechanisms of labile P that vary from the solid sediment phase to the solution phase due to the water–level fluctuations; and 3) clarify the influence mechanism of lake water–level variation on the remobilization of labile P controlled by Fe^{2+} and S^{2-} variation in sediment which can potentially deteriorate the water quality.

2. Material and methods

2.1. Sample collecting and processing

Sediment cores beneath undisturbed overlying water were carefully taken from three representative regions (1#, 2#, and 3#) in Shijiuhu Lake (31°23′~31°33′ N, 118°46′~118°58′ E), a freshwater shallow lake located in the lower Yangtze River basin, Eastern China (Fig. 1), using columnar sampler in October 2020. This lake is connected to the Yangtze River, the third largest river in the world, through the Guxi River, and the water level frequently varies because of the variation in irrigation of the Yangtze River along with seasonal rainfall. The lake has its highest water depth of more than

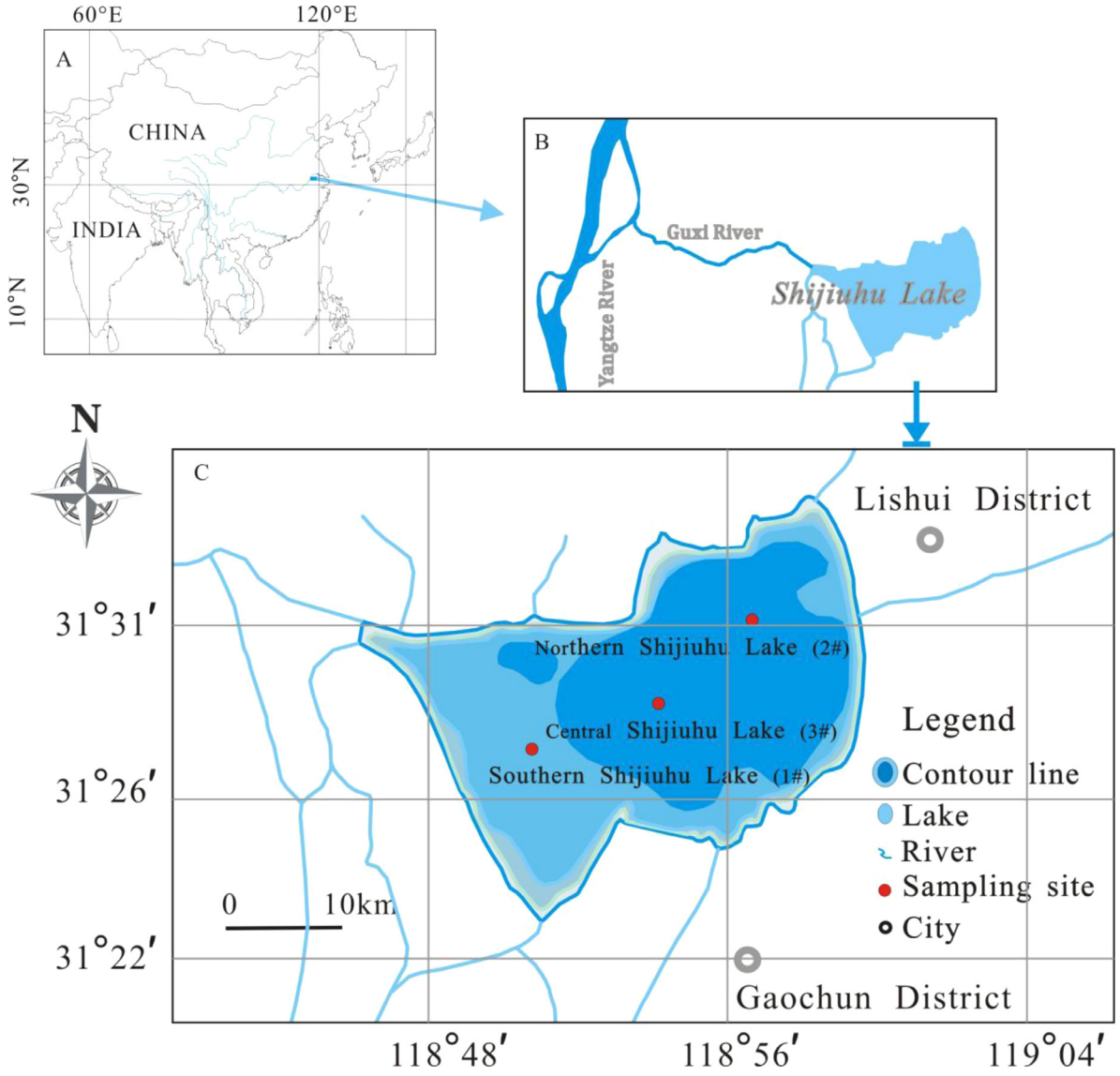

Fig. 1. Sampling sites and location of research region.

6 m in the wet season and can dry up in some regions in low-water seasons (Chi et al., 2016). Excessive nutrients including P are discharged into this lake through runoff and/or river inputs due to increasing anthropogenic activities such as agricultural practices, wastewater discharge, and aquaculture. Overlying water samples were collected simultaneously from the sampling sites. One set of collected sediment columns was carefully sliced into pieces at 1 cm intervals after sampling. The sub-samples were placed in a cooler and transferred to the laboratory where they were kept at 4 °C. After freeze-drying with a vacuum freeze dryer and grinding with an agate mortar , the sediment particles were sieved using a 100-mesh sieve before subsequent analysis. Additionally, two other undisturbed sediment columns were transferred to the lab and used for DGT deployment and incubation experiments, respectively.

Physicochemical parameters of the lake water were observed simultaneously by using a portable water quality analyzer (HACH SL1000, Japan) in field. These included values of water depth (WD), temperature (T), pH, DO, Eh, and electrical conductivity (EC). The concentrations of SRP and total phosphorus (TP) in the overlying water were detected by using molybdenum blue colorimetry (Ruban et al., 2001). Obtained data are listed in Table 1.

2.2. Extraction of P fractions

Different P fractions in pristine sediment cores were extracted based on the sequential extraction method, using the operationally defined standards, Measurements and Testing Programme (SMT) for its ease of use and reproducible results (Ruban, 1999, 2001). This procedure has been developed based on the comparisons of existing schemes and interlaboratory studies (Ruban et al., 2001). Briefly, 0.2 g of freeze-dried sediment was vibrated and extracted with different chemical extractants step-by-step at a constant solid/solution ratio (1:100) (Fig. S1). The modified SMT protocol categorized the sedimentary P phases in the sediment into six independent pools, as follows: $MgCl_2$-P (labile P pool); Fe-P (P bound to Fe and Al oxy(hydr)oxides); Ca-P (P associated with Ca), Pi (total inorganic P); Po (total organic P); and TP (total P). All the phosphate concentrations in the extractant of the six pools were measured using molybdenum blue colorimetry.

Finally, interstitial water in the pristine sediment cores was obtained using centrifugation at 2500 × g for 30 min. The concentrations of SRP in pore water filtered through 0.45 μm GF/C filter membrane (Whatman USA) were immediately detected using molybdenum blue colorimetry (Ruban et al., 2001).

Table 1
Physicochemical parameters in the overlying water of pristine and incubated microcosms from different sampling sites.

Sampling site	location	WD(m)	DO(mg L^{-1})	Eh(mV)	pH	TP(mg L^{-1})	SRP(mg·L^{-1})
1#	31°26′36.44″N,118°50′39.96″E	2.5(0.6)[a]	8.2(7.6)	322(208)	7.32(8.05)	0.06(0.054)	0.024(0.021)
2#	31°28′16.60″N,118°53′16.93″E	4.5(0.6)	6.3(7.5)	331(256)	7.49(8.75)	0.04(0.065)	0.023(0.019)
3#	31°30′13.59″N,118°56′39.01″E	6.5(0.6)	7.2(7.5)	315(242)	7.61(8.48)	0.04(0.052)	0.023(0.018)

[a] The number in bracket is the water level in incubation experiments and the measured values.

2.3. ^{57}Fe-Mössbauer spectroscopy

For the identification and assessment of solid Fe phases, the ^{57}Fe Mössbauer spectra of pristine solid sediment were detected at room temperature (RT) at various depth intervals. The spectra were obtained using a liquid helium bath cryostat connected to a conventional spectrometer (Wissel MS-500, Germany). A ^{57}Co(Rh) source was used with an activity of 25 mCi. The result was obtained by comparing with a 25 μm α-Fe absorber at room temperature. Transmitted radiation was observed using an Ar-Kr proportional counter. Finally, a 512 channel analyzer was used to document the generated signal.

2.4. Analysis of TOC, TN and stable isotopes

Approximately 0.5 g of dried sediment was digested using extractant of mixed nitric acid (HNO_3), hydrochloric acid (HCl), and perchloric acid ($HClO_4$). Subsequently, the total concentrations of elements Al, Fe, Ca, and Mn were measured with inductively coupled plasma atomic emission spectrometry (ICP-AES Profile DV, USA). Another 1 g of freeze-dried sediment sample was treated using 5% HCl solution for the removal of carbonates. Following freeze-drying, the ground sediment was packaged in high-purity tin capsules, and the concentrations of total organic carbon (TOC) and total nitrogen (TN) were simultaneously detected with a CHNS/O elemental analyzer connected to a thermal conductivity detector (EuroVector Euro EA 3000, Italy). The mass ratio of TOC and TN (C/N) in each sediment layer was subsequently calculated.

In addition, values of stable isotopes (δ^{13}C and δ^{15}N) in the pristine sediment core were acquired by using a continuous-flow isotope-ratio mass spectrometer (253Plus, Thermo Fisher Scientific, USA) combined with an elemental analyzer (Flash EA 1112, Thermo Scientific, USA). Ground dried sediment samples (about 20 mg) were put into ultra-pure tin capsules. The prepared samples were successively combusted at 1020 °C in the front furnace and at 700 °C in the rear furnace, respectively. The generated CO_2 and N_2 were isolated from the combustion products for subsequent measurement of isotope values. The δ^{13}C and δ^{15}N of the samples were calculated by comparing to international standards (Vienna Pee Dee Belemnite (VPDB) for C and atmospheric nitrogen for N, respectively) (Abreu et al., 2006).

2.5. Incubation experiment with controlling water depth

Manipulation experiments were performed in the laboratory to explore the dynamic variation of analytes in lake water-sediment interfaces of lakes that are undergoing water-level fluctuation. A set of undisturbed sediment cores were plugged using rubber plugs drilled with small holes to avoid the evaporation of overlying water. The depth of sediment column's overlying water was preserved at low water level (60 cm), which is much lower than the water depth of the lake in the field. The columns were wrapped in foil to stop light entering and preserved at room temperature without disturbance for 30 days. Physicochemical parameters from the incubation microcosm, including DO, T, and pH values of overlying water were measured with a portable water quality analyzer (HACH SL1000, Japan) after the incubation period. The concentrations of total P and SRP in the overlying water were detected with molybdenum blue colorimetry after filtration through 045um filter membrane.

2.6. DGT deployment

The pristine sediment collected from Shijiuhu Lake and the 30-day incubated sediment cores were analyzed using DGT techniques to measure labile SRP, S^{2-}, and Fe^{2+} fluxes and concentrations across the water–sediment interface. In brief, the integrated double-sided Zr-oxide DGT and ZrO-CA DGT devices (EasySensor, China) were aerated using pure N_2 flow for 12 h for deoxidation. Then the devices were perpendicularly penetrated into sediment cores without disturbing the water–sediment interface and experienced an equilibrium period of 24 h for diffusion in the microcosm. Relative to independent Zr-oxide DGT and ZrO-CA DGT devices, this integrated double-sided DGT device has the advantage of synchronous measurement and thus less destruction to the pristine sediment samples. These assemblies were used for high-resolution *in-situ* measurement of labile P (using Zr-oxide DGT), and S^{2-} and Fe^{2+} fluxes (using ZrO-CA DGT), respectively. After the equilibrium period, the DGT devices were removed from the microcosms. The gel surfaces were carefully rinsed using deionized (DI) water to remove the affixed particles. The temperature of the overlying water was synchronously measured for the calculation of diffusive fluxes of the analytes at the water–sediment continuum.

The DGT equipment was then separated into independent Zr-oxide DGT and ZrO-CA DGT devices After rinsing, the masses of elements P and S that had accumulated in the binding gels were determined separately according to the modified coloration–CID method proposed by Ding et al. (2015). In brief, the gel surface of the ZrO-CA DGT device was carefully dried with filter paper, and then scanned with a flat-bed scanner (Canon 5600F, Japan) at 600 dpi resolution equal to a pixel size of 42 μm × 42 μm. The obtained image was subsequently converted into grayscale intensity for the acquisition of high-resolution 2D $S^{2-}{}_{DGT}$ fluxes. Subsequently, the surface of the gel was immediately washed again using DI water, and then cut into small strips at 2-mm intervals. These strips were placed into the centrifuge tubes and subsequently extracted using 1.0 mol L^{-1} HNO_3 for 24 h (Chen et al., 2017). The $Fe^{2+}{}_{DGT}$ concentration in each extract was measured using phenanthroline colorimetric methods (Xu et al., 2013).

Additionally, each gel of Zr-oxide DGT was heated using a hot plate at 80 °C for 24 h, then moistened using the mixed molybdenum reagent for coloration for 1 h at 35 °C. The DGT staining assembly was then rinsed and soaked with cool DI water at 4 °C to avoid the development of color. The surface of the dyed hybrid film was subsequently scanned at 600 dpi resolution using the flatbed scanner described above to obtain high-resolution 2D flux images of labile P_{DGT}. The grayscale intensities of the images following conversion into monochrome were acquired with ImageJ software.

Finally, the calibration curves of the coloration-CID were calculated by analyzing DGT pistons containing S^{2-} and PO_4^{3-}-P in different concentrations (Han et al., 2017). The calibration curves between accumulated masses of P and S in the gel films and

grayscale intensities of corresponding analytes were fitted as exponential equations (Xu et al., 2013). Finally, the grayscale intensities of scanned images from sediment samples were used to calculate accumulation mass of S^{2-} and SRP for each pixel, according to the observed calibration equations.

2.7. Apparent diffusive flux calculation

The apparent diffusive flux across the water–sediment interface can represent the diffusion extent and direction of ions between the surficial sediment and overlying water (Ding et al., 2015). The total diffusive flux was calculated as the sum of the fluxes from the sediments and the overlying water toward the water–sediment interface, respectively. This total flux can be calculated as in eq. 1.

$$J = J_w + J_s = -D_w\left(\frac{\partial C_{DGT}}{\partial x_w}\right)_{(x=0)} - \varphi D_s\left(\frac{\partial C_{DGT}}{\partial x_s}\right)_{(x=0)} \quad (1)$$

where J is the vector sum of the fluxes (μg cm^{-2} s^{-1}) of labile analytes (SRP, Fe^{2+}, and S^{2-}, etc.) in the overlying water and surficial sediment. Jw and Js represent the fluxes (μg cm^{-2} s^{-1}) of analytes diffusing toward the water–sediment interface from the overlying water and sediment, respectively. $(\partial C_{DGT}/\partial xw)_{(x=0)}$ and $(\partial C_{DGT}/\partial xs)_{(x=0)}$ are the concentration gradients of different analytes in the overlying water and the sediment, respectively, φ is the porosity of the surface sediment, and D_w and D_s represent the diffusion coefficients (cm^2 s^{-1}) (Li and Gregory, 1974; Ullman and Aller, 1982).

2.8. DIFS model simulation

A one-dimensional (1D) DIFS model can be used to explore the diffusion kinetics of contaminants in the sediment system, and exchange processes between pellets and DGT devices. Hypothetical dimensionless R values (eq. 2) can describe the resupply capacity of the analytes at the solid/solution interface. The DIFS model can also characterize the dependence extent of R values on diffusion capacity of labile P from solid particle toward the solution (Lehto et al., 2008). This resupply process is composed of both the diffusion of labile P to the DGT surface and its further accumulation into the resin gel through the diffusion layer (Alexa et al., 2009).

$$R = \frac{C_{DGT}}{C_{PW}} \quad (2)$$

where C_{DGT} is the concentration (μg L^{-1}) of the labile fraction of analytes such as labile P detected using the DGT technique, and C_{PW} represents the SRP concentration (μg·L^{-1}) in interstitial water acquired using the centrifugation method. The required parameter values for DIFS model fitting of pristine sediment columns from different sampling sites within 5 cm depth, including diffusion layer thickness (Δg), deployment time (T), diffusion layer porosity (φ_d), diffusion layer diffusion coefficient (D_0), sediment porosity (φ_s), sediment diffusion coefficient (D_s), and particle concentration (P_c) ae listed in Table 2.

The exchange of labile P between the sedimentary solid phase and the solution phase is governed by first order kinetics. The governing equations are composed of a pair of linked partial differential equations eq. 3–(4) (Harper et al., 2000). Other important kinetic remobilization parameters for DIFS model–fitting for sediment systems used to quantify adsorption/desorption kinetics are calculated as in eq. 5–6 (Wu et al., 2016).

$$\frac{\partial C}{\partial t} = -k_1 C + K_{-1} P_c C_s + Ds\frac{\partial^2 C}{\partial x^2} \quad (3)$$

$$\frac{\partial C_s}{\partial t} = \frac{k_1 C}{P_c} - K_{-1} C_s \quad (4)$$

$$K_d = \frac{C_s}{C_{PW}} = \frac{1}{P_c}\cdot\frac{k_1}{k_{-1}} \quad (5)$$

$$T_c = \frac{1}{k_1 + k_{-1}} \quad (6)$$

where K_1 and K_{-1} are sorption constant and desorption rate constants (s^{-1}) of sediment particles for P, respectively. P_c represents the concentration (g cm^{-3}) of particles in sediment. Cs denotes the concentration (mol cm^{-3}) of SRP in the solid sediment phase. K_d is the distribution coefficient of the labile P fraction. T_c represents the response time of DGT deployment (Harper et al., 2000).

2.9. Quality assurance and data plotting

The 2D and 1D spatial distributions of the P_{DGT}, $S^{2-}{}_{DGT}$, and $Fe^{2+}{}_{DGT}$ fluxes and concentrations across the water–sediment continuum were plotted with OriginPro 2017 64Bit (OriginLab Inc., USA). SPSS 20 for Windows (SPSS Inc., USA) was used for statistical analysis.

3. Results

3.1. Physicochemical parameters in sediment and pore water

The values of common physicochemical parameters including TP and SRP concentrations in overlying water did not show significant change between pristine and incubated water–sediment systems (Table 1). Fig. 2 depicts the metal elements (Fe, Al, Ca, and Mn), TOC, and TN concentrations, and ^{13}C, ^{15}N isotope values in pristine sediment particles. The SRP concentrations in pristine pore water and the C/N values of solid sediment are also given in Fig. 2. Generally, the concentrations of metal elements decreased in the order Al > Fe > Ca > Mn across the sediment profiles. Relatively unordered variation of these metal elements existed in the majority of the layers of the sediment columns especially for Fe, Al and Ca, except for few outliers. Significant upward increases of TOC and TN concentrations were found for all the sampling sites through the entire set of sediment columns. C/N varied from 8.0–11.0 and had an adverse variation trend that decreased upwards toward the upper layer. The values of $\delta^{13}C$ and $\delta^{15}N$ for all three sediment columns were −40.0 to −22.7‰ and 3.0 to 8.1‰, respectively, and these overall reduced upward from the bottom layer. Additionally, SRP concentrations in pore water fluctuated in the range of 013–0.44 mg L^{-1}, which was about 10 orders of magnitude higher than in the overlying lake water.

3.2. Variation of p fractions in the sediment profiles

Fig. 3 presents the concentrations and variation of different P fractions in the profiles of pristine sediment from different sites of the lake, extracted using the improved SMT method. In general, TP concentrations at the three sites varied from 292.1 to 644.5 mg kg^{-1} across the whole profiles. More significant fluctuation of TP values were found at sites 2# and 3# than at 1#. Generally, total Pi, with values varying from about 160−490 mg kg^{-1}, was higher than total Po in all sediment profiles. A similar change in trend of Pi to TP existed at all three sites. The Po concentrations on the sediment profiles (except that from site 1#) displayed an obvious increase from the bottom upward toward the top layer. The Pi pools in the three sampling sites represented the relatively homologous

Table 2
Calculated input values of parameters in sediment at 5 cm depth involved in DIFS model.

Site	Depth Cm	Δg [a] cm	T [b] h	φ_d [c] –	φ_s [d] –	D_0 [e] $cm^2\ s^{-1}$	D_s [f] $Cm^2\ s^{-1}$	P_c [g] $g\ cm^{-3}$
1#	1	0.09	24	0.75	0.866	5.74E-06	4.461E-06	0.409
	2	0.09	24	0.75	0.852	5.74E-06	4.346E-06	0.461
	3	0.09	24	0.75	0.842	5.74E-06	4.275E-06	0.495
	4	0.09	24	0.75	0.837	5.74E-06	4.235E-06	0.515
	5	0.09	24	0.75	0.823	5.74E-06	4.128E-06	0.571
2#	1	0.09	24	0.75	0.915	5.74E-06	4.870E-06	0.248
	2	0.09	24	0.75	0.888	5.74E-06	4.640E-06	0.333
	3	0.09	24	0.75	0.881	5.74E-06	4.583E-06	0.356
	4	0.09	24	0.75	0.857	5.74E-06	4.388E-06	0.442
	5	0.09	24	0.75	0.831	5.74E-06	4.188E-06	0.539
3#	1	0.09	24	0.75	0.865	5.74E-06	4.452E-06	0.413
	2	0.09	24	0.75	0.856	5.74E-06	4.378E-06	0.446
	3	0.09	24	0.75	0.867	5.74E-06	4.469E-06	0.405
	4	0.09	24	0.75	0.841	5.74E-06	4.261E-06	0.502
	5	0.09	24	0.75	0.802	5.74E-06	3.981E-06	0.655

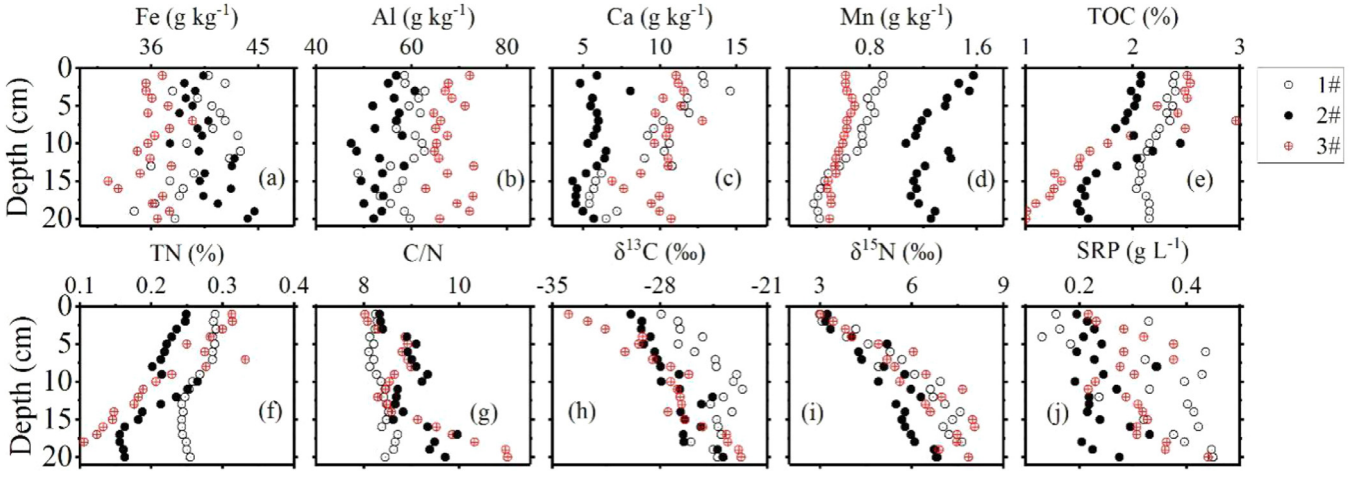

Fig. 2. Physic-chemical parameters of different layers of sediment columns from the three sampling sites.

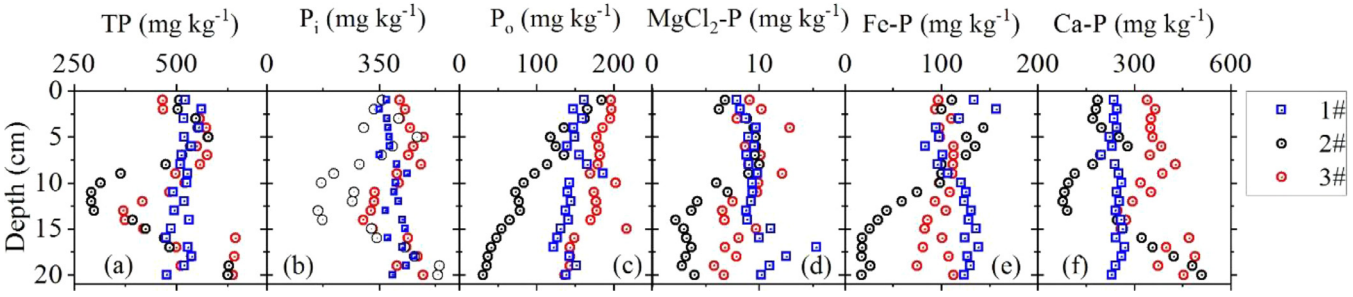

Fig. 3. P fractions in different layers of sediment columns from the three sampling sites.

variation among the entire profiles; that is, $MgCl_2$-P < Fe-P < Ca-P. Meanwhile, Ca-P concentrations accounted for the largest fraction of the TP, at 30.0–80.0%. Fe-P constituted a second largest Pi pool with about 14.6–28.8% of TP concentration. Labile $MgCl_2$-P contributed the fraction less than 3% of TP. Significantly, a stable ratio of Fe-P accounting for TP was measured at site 1# compared with the two other sites, especially site 2# which had increasing values from the bottom toward the upper layers.

Also at site 2#, significant upward increases of $MgCl_2$-P and Fe-P were found from the bottom layer to about 10 cm depth, then concentrations of these two pools did not obviously fluctuate until the surface layer. However, these two P pools at sites 1# and 3#, with lower water depth kept relatively stable across the entire sediment depth. Adverse variation of Ca-P at site 2# was detected below 10 cm depth except for a few outliers. Generally, the $MgCl_2$-P, Fe-P, and Ca-P at site 1#, which underwent intensive water level fluctuation relative to the two other sampling sites, maintained more analogous concentrations across the entire sedimentary profiles.

3.3. ^{57}Fe Mössbauer spectroscopy for solid sediment particles

The result of Mössbauer spectroscopy at room temperature for different sediment depths are shown in Fig. 4. Modeling was implemented using the Lorentzian line shape model. The proportion of Fe fraction was calculated as area of individual peak compared with total Fe phases. The obtained data about solid Fe mineralogy phases are presented in Table 3. The main Fe minerals including Fe(III) minerals (ferrihydrite) and phyllosilicate concomitant Fe(II) minerals (siderite and/or chlorite), were distinguished in all the

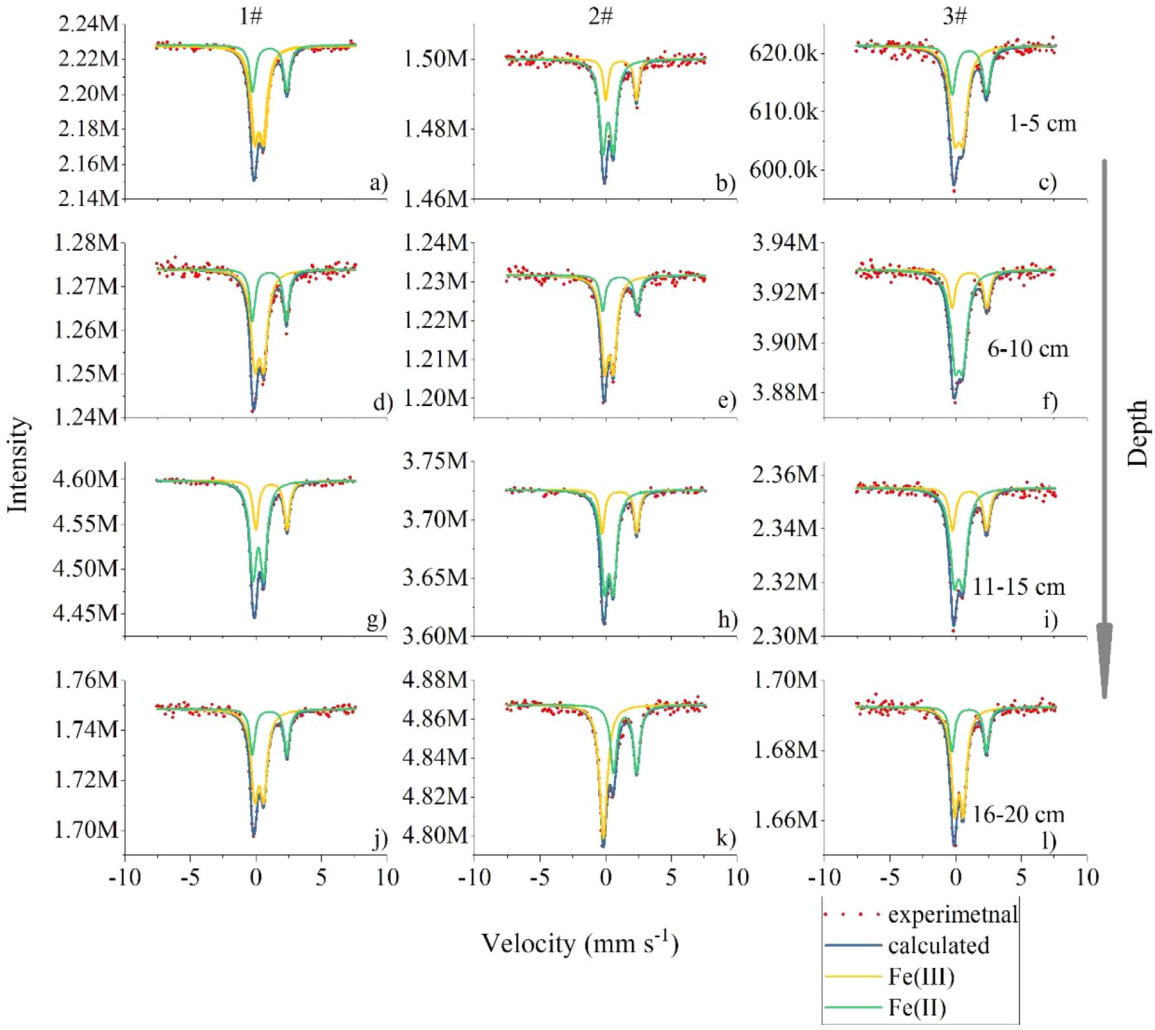

Fig. 4. Mössbauer spectra of mixed sediment layers at room temperature. The dotted and colored lines represent measured experimental data and relative contributions of different Fe phases, respectively. The spectra were fitted using Lorentzian line shapes with the least squares method.

sediment samples (Murad and Cashion, 2004; Yuan et al., 2019). Fe(III) phase concentrations were approximately 2.5 orders of magnitude higher than Fe(II) phase concentrations. Similar Fe(II) percentages (70.2–74.7%) accounting for total Fe kept relatively stable at different sedimentary depths except for a few outliers. Generally, comparable ratios of Fe(II) percentages were found at all three different research sites, although slight variations also existed between different sites and depths.

3.4. Variation of 2 D patterns of P_{DGT} and $S^{2-}{}_{DGT}$ through the water–sediment interface before and after incubation

High-resolution *in-situ* 2D and 1D images, gained by using the Double-sided DGT technique of P_{DGT} and $S^{2-}{}_{DGT}$ fluxes across the water–sediment interface before and after incubation are shown in Figs. 5 and 6a–f. Greater fluxes were simultaneously detected in the water–sediment continuum at site 1# compared with the other two sites. The lowest fluxes of P_{DGT} and $S^{2-}{}_{DGT}$ were found at site 2#. Note that generally significant variation in gradients of P_{DGT} and $S^{2-}{}_{DGT}$ fluxes across the sediment column were detected at approximately 5 cm depth. In addition, P_{DGT} concentrations kept relatively stable at about 0.064±0.006, 0.053±0.006, and 0.031±0.006 mg L^{-1} at sites 1#, 2#, and 3#, respectively, from the bottom sedimentary layer upwards to about 5 cm depth, then sharply decreased to about 0.002 mg L^{-1} until the water-sediment interface. $S^{2-}{}_{DGT}$ concentrations maintained relatively stable at about 0.16±0.02, 0.17±0.04, and 0.13±0.01 mg L^{-1}, respectively, at the three sampling sites, again until about 5 cm depth, then rapidly decreased to about 0.013, 0.05, and 0.05 mg L^{-1} in the top sediment layer. The variation measured by DGT indicated that the fluxes and concentrations of P_{DGT} and $S^{2-}{}_{DGT}$ significantly decreased in the three microcosms after incubation with low water levels, especially in the top 5 cm depth layer of sites 1# and 3#. Between 5 cm depth and the water–sediment interface, P_{DGT} concentrations experiencing incubation fell to less than half those of the pristine sediment columns. $S^{2-}{}_{DGT}$ concentrations decreased to less than 0.1 mg L^{-1}at about 5 cm layer, and further reduced to 0.01 mg L^{-1} at the water–sediment interface.

3.5. Variation of 1D distributions of Fe^{2+} through the water–sediment interface before and after incubation

Fluxes of analytes can be converted to concentration in binding gel (C_{DGT}) according to Fick's first law and reflected diffusive potential in sediment, pore water, and DGT binding gel (Alexa et al., 2009). Fig. 6g–I illustrates the 1D variation of $Fe^{2+}{}_{DGT}$ concentrations through the water–sediment interface. Similar to the variations of P_{DGT} and $S^{2-}{}_{DGT}$, the $Fe^{2+}{}_{DGT}$ concentrations generally remained stable below 5 cm depth, with average values of 4.9, 3.2, and 2.6 mg L^{-1}, respectively, at the sampling sites 1#L, 2#L,

Table 3
Mössbauer fitting parameters and measured Fe fraction for different layers of sediment column from different sampling regions using ^{57}Fe Mössbauer spectroscopy at room temperature.

Depth	Magnetic splitting	Amplitude	δ [a](mm s^{-1})	ΔE_Q [b](mm s^{-1})	Line width	Valence state	Area(%)
			1#				
1–5 cm	Doublet 1	46,754.1	0.24	0.68	0.73	Fe(III)	70.5
	Doublet 2	26,532.1	1.04	2.61	0.54	Fe(II)	29.5
6–10 cm	Doublet 1	19,589.6	0.25	0.68	0.71	Fe(III)	70.2
	Doublet 2	11,797.3	1.01	2.59	0.50	Fe(II)	29.8
11–15 cm	Doublet 1	99,504.3	0.18	0.81	0.63	Fe(III)	69.6
	Doublet 2	54,682.9	1.17	2.37	0.50	Fe(II)	30.4
16–20 cm	Doublet 1	31,771.2	0.24	0.68	0.66	Fe(III)	70.6
	Doublet 2	18,344.0	1.03	2.63	0.47	Fe(II)	29.4
			2#				
1–5 cm	Doublet 1	24,268.2	0.18	0.79	0.61	Fe(III)	74.7
	Doublet 2	11,742.1	1.16	2.34	0.43	Fe(II)	25.3
6–10 cm	Doublet 1	21,833.4	0.25	0.67	0.63	Fe(III)	75.4
	Doublet 2	9184.6	1.07	2.63	0.48	Fe(II)	24.6
11–15 cm	Doublet 1	77,207.1	0.24	0.67	0.62	Fe(III)	74.1
	Doublet 2	37,246.1	1.04	2.63	0.45	Fe(II)	25.9
16–20 cm	Doublet 1	35,138.3	0.19	0.10	0.67	Fe(III)	54.3
	Doublet 2	34,504.4	1.47	1.76	0.57	Fe(II)	45.7
			3#				
1–5 cm	Doublet 1	13,449.3	0.23	0.65	0.83	Fe(III)	67.3
	Doublet 2	8333.9	1.03	2.61	0.65	Fe(II)	32.7
6–10 cm	Doublet 1	32,196.9	0.24	0.61	0.79	Fe(III)	74.6
	Doublet 2	15,256.8	1.04	2.65	0.57	Fe(II)	25.4
11–15 cm	Doublet 1	30,525.5	0.22	0.68	0.76	Fe(III)	71.3
	Doublet 2	15,815.3	1.05	2.60	0.59	Fe(II)	28.7
16–20 cm	Doublet 1	26,917.5	0.25	0.66	0.61	Fe(III)	72.5
	Doublet 2	12,743.7	1.02	2.62	0.48	Fe(II)	27.5

[a] Isomer shift.
[b] Quadrupole splitting.

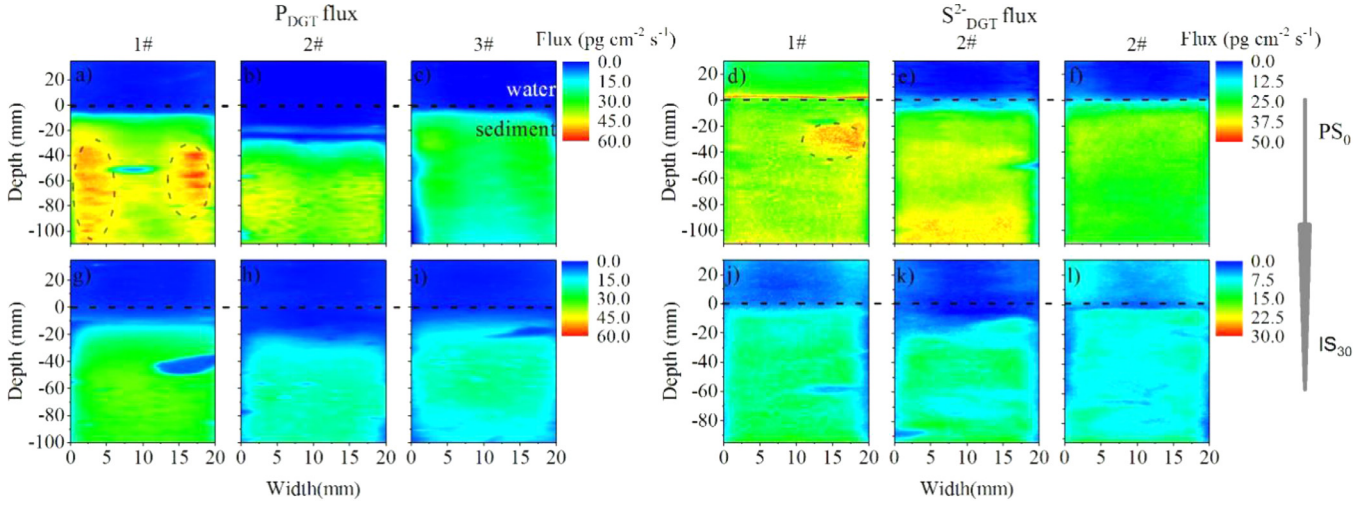

Fig. 5. Variation of high-resolution 2D images of P_{DGT} and $S^{2-}{}_{DGT}$ fluxes in the water–sediment continuum before and after incubation episode after 30-day from the three sampling sites. The black dashed lines indicate the water–sediment interface (WSI). PS_0 and IS_{30} refer to the pristine sediment and incubated sediment, respectively.

and 3#. The concentrations drastically decreased to 0.5, 0.1, and 0.01 mg L^{-1}, respectively, from about the 5 cm layer upward to the top layer. The $Fe^{2+}{}_{DGT}$ values obviously decreased to 2.9, 2.6, and 1.4 mg L^{-1} below 5 cm depth, and kept relatively steady toward the 5 cm sedimentary depth at all of the sampling sites. Then the concentrations dramatically reduced to 0.4, 0.2, and 0.03 mg L^{-1}, respectively, upward towards the top layer of the sediment. Additionally, the $Fe^{2+}{}_{DGT}$ concentrations in overlying water at site 1# were distinctly higher than those of the other two sediment cores. Generally, roughly analogous changes were measured in all of the sampling sites. However, site 1#, with high fluctuations of water level, displayed more significant variations of $Fe^{2+}{}_{DGT}$ concentrations compared with the two other sites with relatively high water depth.

3.6. Diffusion fluxes of SRP, S^{2-} and Fe^{2+} through the water–sediment interface

Apparent diffusion fluxes of P_{DGT}, $S^{2-}{}_{DGT}$, and $Fe^{2+}{}_{DGT}$ across the water-sediment continuum of the three sampling sites of the lake are shown in Fig. 7. Obviously positive flux values of these parameters were determined at all the research sites. The highest fluxes of P_{DGT} and $Fe^{2+}{}_{DGT}$ in pristine sediment cores, up to 0.015 and 1.3 μg (cm^2 s) $^{-1}$, respectively, were found in sampling site 1#. Higher $S^{2-}{}_{DGT}$ fluxes were also monitored at site 1#. It is noteworthy that the diffusion fluxes of all the parameters through the water–sediment interface distinctly decreased with the execution of the incubation experiments for all the sampling sites.

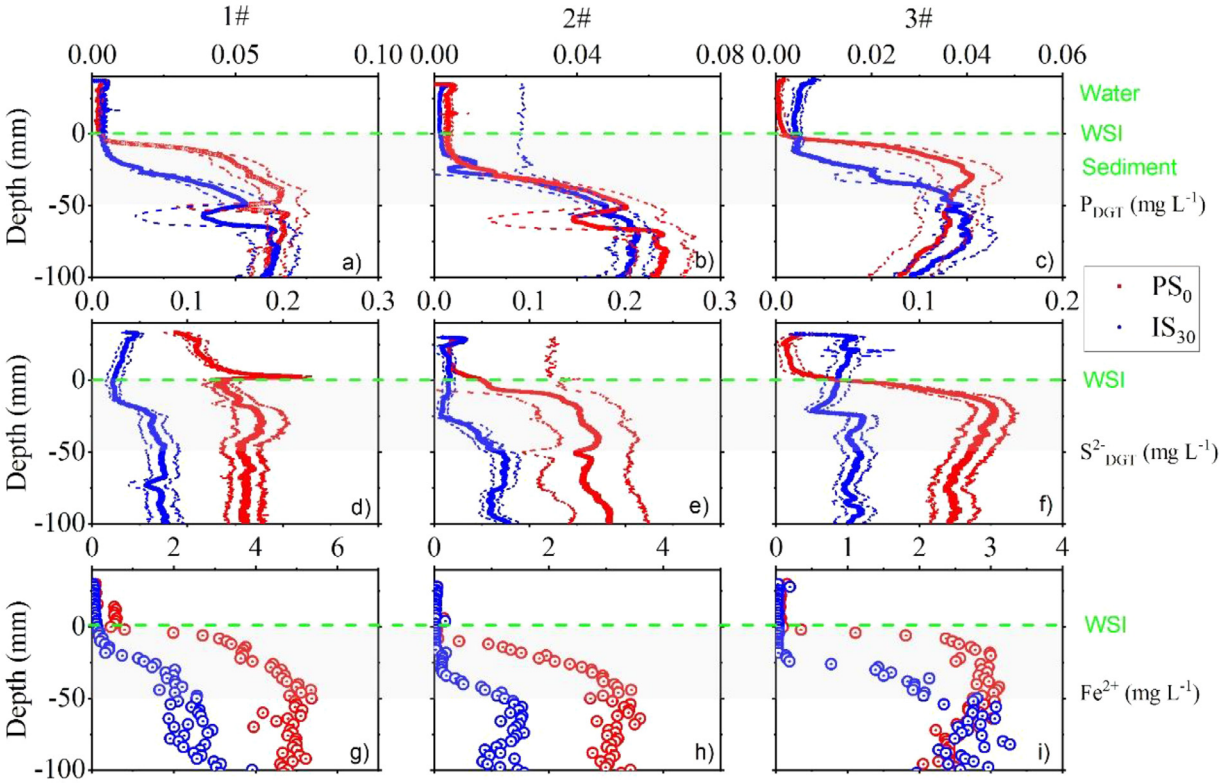

Fig. 6. Variation of high-resolution 1D profiles of SRP_{DGT}, $S^{2-}{}_{DGT}$ and $Fe^{2+}{}_{DGT}$ fluxes obtained using DGT in the water–sediment continuum before and after the 30-day incubation from the three sampling sites. The green dashed lines indicate the WSI. The light gray region shows the significant variation depth (ca. 5 cm) on the sediment profiles of individual analytes.

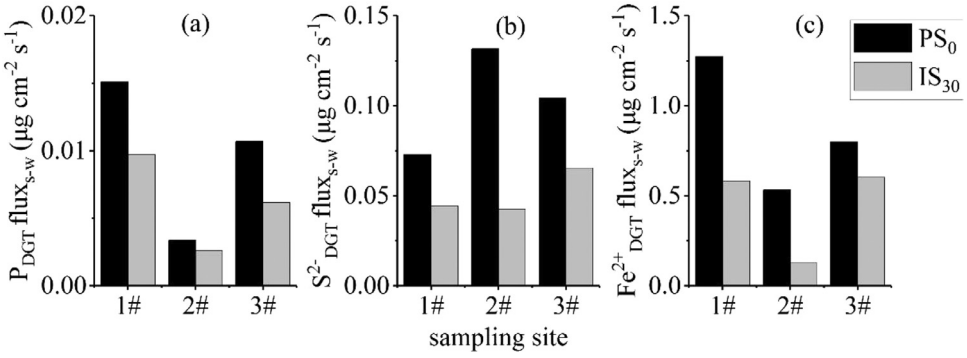

Fig. 7. Diffusion fluxes of P_{DGT}, $S^{2-}{}_{DGT}$, and $Fe^{2+}{}_{DGT}$ across the WSI before and after the 30-day incubation at each sampling site.

4. Discussion

4.1. Fe bound P dominates the mobility of P in the sediment

Partition of P fractions indicates the different mobility and resupply potential of P from the solid sediment to the aqueous solution. $MgCl_2$-P, which is associated with the solid surface and the compound by weak physical and chemical interactions, can be directly adsorbed by aquatic organisms as the most labile P pool (Aminot and Andrieux, 1996). This implies the resupply potential of labile P to the solution phases even when the concentrations of this pool are relatively low compared with other P fractions. Gradually increasing $MgCl_2$-P concentrations from the bottom toward the top layer especially at sites 1# and 3# suggested the accumulation of this kind of P phase in the upper layer of sediment. This tendency was also observed in other aquatic environments such as Lake Erken (Rydin, 2000), Lake Taihu (Yuan et al., 2019), and the Peru Margin (Jaisi and Blake, 2010). However, inverse decreasing trends on the sediment profiles were detected in other water bodies, such as Chesapeake Bay, etc. (Joshi et al., 2015). These results may be attributed to differences in resupply dynamics of labile P pools. Additionally, research site 1# displayed relative stability and homogeneity of labile $MgCl_2$-P concentrations across the whole sediment column except for a few outliers. All these variation characteristics suggested different bonding effects on the surface of sediment particles between free phosphate and fixed P-containing minerals, which consequently controlled sorption–desorption processes under various conditions including fluctuating water depth.

Significant increases of Fe-P upward from the bottom layer were observed in site 2#, which had the highest water level, indicating it was the most stable burial environment in this lake. Low values of Fe-P suggested a reduced layer with low redox

potential under the thin oxidized zone, where P bound to ferric (oxy)hydroxides (FeO(OH)) may be released due to the reduction of ferric ions to ferrous ions inducing the decrease of particle P (Borch et al., 2007). An upward increasing trend of this kind of P phase was normally investigated in aquatic ecosystems without dramatic variations of water level (Ruban et al., 1999; Liu et al., 2019). Under anoxic/anaerobic conditions, Fe(III) can be reduced to Fe(II) as electron acceptor and consequently dissolves in the water phase together with the release of phosphate in the deep layer of the sediment (Aminot and Andrieux, 1996). The most significant positive correlations (R^2=0.927, P<0.01) were observed between $MgCl_2$-P and Fe-P compared with Ca-P in sediment of site 2#, indicating that the Fe-P phase potentially contributes to the deposition of labile P in steady anoxic conditions with deeper overlying water. It is interesting that the sites 1# and 3#, having relatively lower overlying water levels than site 2# displayed homogeneity in Fe-P concentration across the whole sedimentary depth. Weak correlation between $MgCl_2$-P and Fe-P was discovered in sites 1# and 3#. DO can penetrate into surficial sediment when the water is shallow, which may result in the more extensive oxidation of sediment (Kreling et al., 2017). This process favors the re-oxidation of labile Fe(II) into Fe(III) and the corresponding dissociation of phosphate in oxic episodes, which can further lead to the immobilization of P as solid particle P phase in lacustrine ecosystems. Higher SRP concentrations (Fig. 2j) were also detected in pore water of sediment from site 2#, indicating that the Fe-P was mobilized to be desorbed into the aquatic phase into the deep-water environment in anoxic episodes. However, these notions need further direct evidence.

Ca-P accounted for higher ratios (>50%) of Pi, except for a few outliers, across the whole profile in all the sampling sites, compared with potentially mobilizable phases, including $MgCl_2$-P and Fe-P. However, detrital and authigenic -origin Ca-P tended to remain relatively stable in accumulation characteristics during the sedimentation history (Ruttenberg and Berner, 1993). Measurements of phosphate oxygen isotopes ($\delta^{18}O_P$) in the sediment from different aquatic environments also revealed that Ca-P possessed lighter isotope values (Joshi et al., 2015; Yuan et al., 2019). This demonstrated that Ca-P was locked in and remained largely unaltered after its formation and precipitation as Ca-containing minerals in the sediment. Weaker correlation detected between Ca-P and mobile $MgCl_2$-P (R^2=−0.429, P<0.05) in site 2# with more stable sedimentary conditions, further suggested the inconspicuous contribution to the mobile P fraction.

Additionally, Po in the sediment from these lake regions accounted for between 5−49% of TP. Increasing Po proportion from the top layer downward indicated the preferential degradation and mineralization into Pi in deeper layers. Po compounds were often considered as part of the refractory P. However, Po compounds were composed of labile fractions which can re-mineralize into the Pi fraction and played a significant role in P cycling (Pant et al., 2002). Po was often present in natural OM from various sources (Bedrock et al., 1995). C/N can be used to speculate the source of OM in the sedimentary particles settling into the lakes (Xia et al., 2021). Plant groups mainly contribute to the lake OM and display different ranges of C/N ratios: algae-derived OM (phytoplankton) typically possesses C/N mass ratios of 4 to 10, while aquatic macrophytes range from 10 to 50, and vascular terrestrial plants generally have values higher than 20 (Contreras et al., 2018). Therefore, C/N varying from 8.0–11.0 in this research suggests the predominantly algae-derived source of OM in the sediment. The decreased trend toward the upper layer suggested the aggravation of algae biomass following the anthropogenic activities around the lake. The low TOC values in the deeper sediment layer might be due to the greater degradation rates of OM under aerobic scenario, rather than anaerobic, conditions (Pant et al., 2002), which induced the degradation of Po in the sediment, especially at site 1# having deeper water. Furthermore, C and N stable isotopes (^{13}C and ^{15}N) are also frequently used to identify the source of OM deposited in the lakes (Li et al., 2018). The decreasing upwards trend of $\delta^{13}C$ and $\delta^{15}N$ values also indicated the alternation of OM sources during sedimentation processes. The $\delta^{13}C$ values of endogenous algae in the lakes normally ranged from −31 to −24‰ (Meyers, 2003). The $\delta^{15}N$ values of macroalgae commonly varied between 0.5 and 13.8 ‰ (Cole et al., 2004). Generally, C/N along with $\delta^{13}C$ and $\delta^{15}N$ illustrated that the increasing algae detritus induced the accumulation of biogenic P-containing OM in the sediment. The degradation of OM and reduction of Fe oxy(hydr)oxides could simultaneously trigger the release of phosphate into the pore water from Po and Fe-P in sediments during the diagenetic processes (Egger et al., 2015). However, it should be noted that the relatively long half-life (several to dozens of years) of Po compounds indicated that the resupply potential of labile P fraction was inconspicuous in the sediment (Ahlgren et al., 2005, 2006; Reitzel et al., 2006; Ding et al., 2013; Yuan et al., 2020). The predominance of Fe-P release within a short time in lacustrine sediment systems contributing to the increase of the labile P fraction in the lakes deserves further consideration and explicit evidence.

Table 4
Calculated output values of R, K_d, T_c, k_1, and k_{-1} for surficial sediments of different sampling sites using DIFS model.

Site	Depth	R	K_d $cm^3\ g^{-1}$	T_c s	k_1 s^{-1}	k_{-1} s^{-1}
1#	1	0.069	57.955	9.999E+06	1.00E-07	4.22E-09
	2	0.219	52.008	9.999E+06	1.00E-07	4.17E-09
	3	0.326	48.646	8.156E+05	1.23E-06	5.09E-08
	4	0.380	78.803	2.429E+05	4.12E-06	1.01E-07
	5	0.349	52.544	3.730e+05	2.68E-06	8.93E-08
2#	1	0.011	35.026	9.999E+06	1.00E-07	1.15E-08
	2	0.026	29.187	9.999E+06	1.00E-07	1.03E-08
	3	0.041	38.654	9.999E+06	1.00E-07	7.26E-09
	4	0.141	45.625	9.999E+06	1.00E-07	4.96E-09
	5	0.175	40.055	9.999E+06	1.00E-07	4.63E-09
3#	1	0.056	36.558	9.999E+06	1.00E-07	6.63E-09
	2	0.135	35.586	9.999E+06	1.00E-07	6.30E-09
	3	0.139	30.943	9.999E+06	1.00E-07	7.98E-09
	4	0.123	30.214	9.999E+06	1.00E-07	6.59E-09
	5	0.097	23.890	9.999E+06	1.00E-07	6.39E-09

4.2. Re-mobilization dynamics of SRP evaluated using the DIFS model

The output values of dynamic parameters for labile P fraction in 5-cm sediment depths, including R, K_d, T_c, k_1, and k_{-1}, were obtained using the DIFS model and are listed in Table 4. The general downward increase of R values at all three sampling sites indicated that phosphate depletion in pore water was supplemented by solid phases for DGT uptake owing to higher labile P concentrations controlled by the reduction of Fe-P in the deeper layers. Higher R values indicated more significant resupply efficiency and potential bio-availability of labile P in the sediment, which further contributed to higher labile P concentrations in the pore water in deeper layers (Monbet et al., 2008). Response time (T_c) generally decreased with depth downward at site 1#, with its low water depth. T_c values are sensitive to the variation of R values in the DIFS model (Lehto et al., 2008). Lower T_c values together with larger R values in this study further demonstrated the significant resupply capacity of labile P from sediment particles to interstitial water when the sediment tends to be anaerobic.

Fig. 8 plots the time-dependence curves of R values for labile P in the 5-cm sediment depth layer, which were principally dominated by both the desorption of sediment particles into the pore

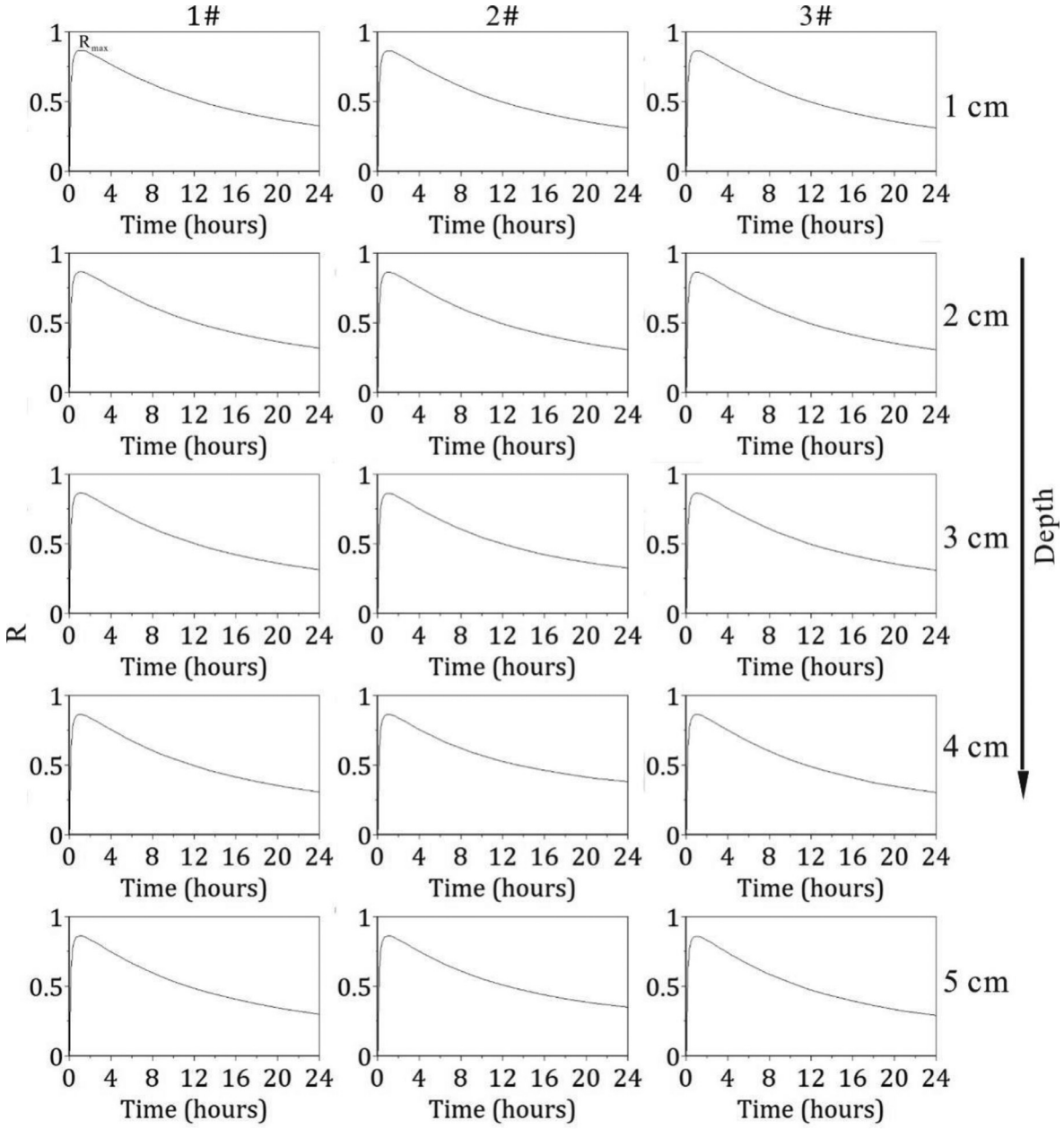

Fig. 8. Time-dependence of R values for different superficial sediment layers (1–5 cm) and model lines fitted using the DIFS model.

water and the accompanying diffusion efficiency to the diffusive layer of the DGT device (Harper et al., 2000; Sochaczewski et al., 2007). The initial increase of R curves may be attributed to the dramatically steep linear diffusion of labile P from the interstitial water toward the diffusion layer of the devices (Lehto et al., 2008). Progressive decline after the peak value of R occurred due to the limit to the resupply induced by the consumption of labile P near the DGT device along with the low desorption rate from the solid sediment phase (Heidari et al., 2017; Guan et al., 2017). R accumulation curves confirmed the considerable re-mobilization and transport capacity of mobile P fractions including Fe-P from the solid sediment to the pore water as well as overlying water via dynamic diffusion. Additionally, K_d can also exert influence on the R values together with T_c. Obvious positive correlation was found between K_d and R (R^2=0.688, $P < 0.01$), which further reflected the remarkable influence of solid sediment exchanging with the solution in the sediment system. Obviously higher k_1 than k_{-1} values suggested stronger adsorption potential rather than desorption for the solid sediment across the whole sediment profiles of the research sites (Heidari et al., 2017).

Generally, higher R values combined with other dynamic parameters indicated that continuous resupply of labile phosphate at deep layers influenced the concentration gradient of labile P, especially at site 1#. This effect was driven by both desorption of mobilizable $MgCl_2$-P and reduction of Fe-P in sediment, especially under anaerobic conditions in deep sediment. This dynamic process was responsible for the increasing concentrations of SRP in overlying water of lacustrine ecosystems. It is noteworthy that lower R values and higher T_c at similar sediment layers were found at sites 2# and 3#, both having higher water levels. This indicated that more significant fluctuations of water depth potentially contributed to the desorption and resupply of labile P from the solid phase to the aqueous solution. However, this speculation needs further research and evidence.

4.3. Potential regulation of Fe-P by water-level fluctuation

Fig. 5 shows the high-resolution 2D variations of P_{DGT} and $S^{2-}{}_{DGT}$ fluxes at the water–sediment interface before and after incubation. Significant decreases of these two analytes were detected after incubation. Fig. 6a–f also depicts the variations of P_{DGT} and $S^{2-}{}_{DGT}$ concentrations through the water–sediment continuum, and exhibits the distinctly reduced trend, especially at sites 1# and 3# with relatively low water depth. Concentrations of P_{DGT} and $S^{2-}{}_{DGT}$ decreased by more than half compared with the pristine sediment columns within a short time (30 days), which was obviously quicker than the known Po mineralization rates (several to dozens of years in natural environments) for the resupply of labile P fractions from solid phase to aqueous solution. In addition, $Fe^{2+}{}_{DGT}$ concentrations also significantly decreased by more than half in each microcosm after the incubation relative to the pristine sediment cores (Fig. 6g–i). This clearly indicated the rapid re-oxidation of Fe(II) ions into Fe(III) and the existence of the solid particle phase due to the reduction of water depth together with an increase of penetration depth of DO in the water–sediment continuum. Synchronous sorption and immobilization of labile phosphate accompanied the shift of Fe(III) and Fe(II) phases due to the oxidation of sediment modified by water depth. Note that more obvious fluctuations in P_{DGT} and $Fe^{2+}{}_{DGT}$ concentrations werefound at about 1–5 cm depth, indicating that the desorption activity principally happened in this sedimentary layer. This active layer depth was slightly deeper than in the existing data (ca. 0.5–10 mm) (Stockdale et al., 2009; Gao et al., 2016; Han et al., 2017), indicating the larger range of resupply source of labile analytes from the deeper layer of sediment that is mediated by water level.

It is interesting that the generally higher P_{DGT} and $Fe^{2+}{}_{DGT}$ fluxes and concentrations were found at site 1#, which had the lowest water depth and highest DO concentration relative to the other sites before and after the incubation experiments. Mössbauer measurements indicated that a relatively higher Fe(II) fraction was generally detected in the sediment column from site 1# (Table 3). It is speculated that more frequent water–level fluctuations due to hydrological and meteorological conditions of the lake basin exerted stronger influence on the Fe phases in those lake regions having shallow water depth (Dijkstra et al., 2014). The comparable Fe(III)/Fe(II) phase ratios to total Fe at different sediment depths supported the frequent fluctuations of water level in this lake, which was significantly different from findings at Taihu Lake which had downward increasing Fe(II) concentrations toward the deeper sediment layer (Yuan et al., 2019). Comparable Fe-P concentrations across the whole sediment profile from site 1# further supported this inference. Nriagu and Dell (1974) proposed that crystalline Fe-containing minerals are remarkably more stable than amorphous ferric phosphate. However, amorphous Fe(II)-containing minerals in association with P, such as chlorite and/or siderite, were formed and preserved in the sediment via the transition of aerobic and anoxic episodes. The investigation of Rozan et al. (2002) indicated that significant amounts of phosphate could be sequestered in amorphous iron phases. This was corroborated by the inconspicuous fluctuation of total Fe concentrations (Fig. 2a) across the whole sediment column. This enrichment action, predominantly controlled by oxygen resupply conditions during the diagenetic process, may have led to higher proportions of both labile P and Fe(II) phase at site 1# experiencing multiple variations even at low-water levels. A higher proportion of crystal Fe(II)-containing minerals existed at sites 2# and 3# with their relatively stabilized deposition environments, which was responsible for the low concentrations of reducible Fe-P and labile Fe(II) phase. These processes contributed to the occurrence of high Fe(II) concentration and subsequent reductive dissolution in the sediment when the DO values in the microcosms were high, under low water-level conditions (Lucotte et al., 1994; Anschutz et al., 1998). The incubation experiments proved that Fe (II) mineral coating by the oxide with P can be desorbed and released into water within a short time, which resulted in the high labile Fe(II) concentration when the water depth became high and caused the reduction scenario (House and Denison, 2000). This desorption and resupply effect for the labile P in the lake water was notably faster than the Po degradation and mineralization effect mentioned in Section 4.1.

Finally, significant decreases of diffusion fluxes of labile P_{DGT} and $S^{2-}{}_{DGT}$ across the water–sediment interface was detected at each microcosm with low overlying water depth after the 30-day incubation compared with pristine sediment (Fig. 5). High-resolution DGT measurements and kinetics calculation demonstrated that the variation of water level can modulate the occurrence of P and Fe phases within a short time scale. The incubation experiments revealed that higher water depth induced the desorption of P bound to Fe-containing minerals into pore water and its accompanying diffusion upward into overlying water, which potentially facilitated the enrichment of labile P mass and fueled the eutrophication in the lake.

4.4. Synergistic regulation of sulfide on P regulation controlled by water depth

Furthermore, obvious decreases of $S^{2-}{}_{DGT}$ fluxes and concentrations were also observed in the sediment, suggesting the rapid re-oxidation of S^{2-} into S° following by $SO_4{}^{2-}$ in oxic episodes at shallow water depth in the microcosm. Reductive dissolution of Fe(III) phases through reactions with sulfide can result in the diffusion of labile P bound to Fe(III)-containing minerals and Fe(II) ions (Eq. (7)) (Küster-Heins et al., 2010; Li et al., 2016). Reduced diffusion fluxes of $S^{2-}{}_{DGT}$ (Fig 5) from the sediment toward the overlying water at all the research locations further suggested the oxidization and fixation of a higher valence state of sulfur due to the decreased water depth. Similar to the results proposed by Sun et al., (2016), remarkable accumulation of S^{2-} with sedimentary depth was detected at about 5 cm depth in the pristine sediment columns, indicating the preferable enrichment of S^{2-} under anoxic conditions. The incubation experiments demonstrated the obvious oxidation of S^{2-} under low water-level conditions and its converse reduction in high water-depth episodes on a short time scale. Sulfide in interstitial water was principally generated from $SO_4{}^{2-}$ reduction as electron acceptor in anaerobic episodes (Naylor et al., 2004; Zhao et al., 2019). The $SO_4{}^{2-}$ reduction can trigger the production of FeS and the acidification of the sediment system, which furthers the activation and desorption of P bound to Fe(III) (oxy)hydroxides in deep layers (Eq. 8) (O'Connell et al., 2015; Norgbey et al., 2020).

$$2FeOOH+3S^{2-}+4H^{+}\leftrightharpoons 2FeS+S^{0}+4H_2O \quad (7)$$

$$Fe_3(PO_4)_2\cdot nH_2O+3S^{2-}+6H^{+}\leftrightharpoons 3FeS+2H_2PO_4{}^{-}+ nH_2O \quad (8)$$

Similarly, by comparing the pristine and incubated microcosms, high-resolution 2D and 1D images of S^{2-} fluxes and concentrations show that the shift from S^{2-} to $SO_4{}^{2-}$ was also accelerated in the sediment–water system via the DO content variation caused by water depth fluctuation. Higher $S^{2-}{}_{DGT}$ fluxes and concentrations were found at site 1#, at the surficial sediment within about 5 cm depth where the chemical action and/or microbial actions including sulfate-reducing bacteria or sulfur-oxidizing bacteria at different DO conditions varied with water depth (Wu et al., 2019). Additionally, the occurrence of S^{2-} in the sediment facilitated the reduction dissolution under hypoxic conditions with the increase of lake water level. In general, our investigations indicated that frequent fluctuations of water depth in the lake over time stimulated

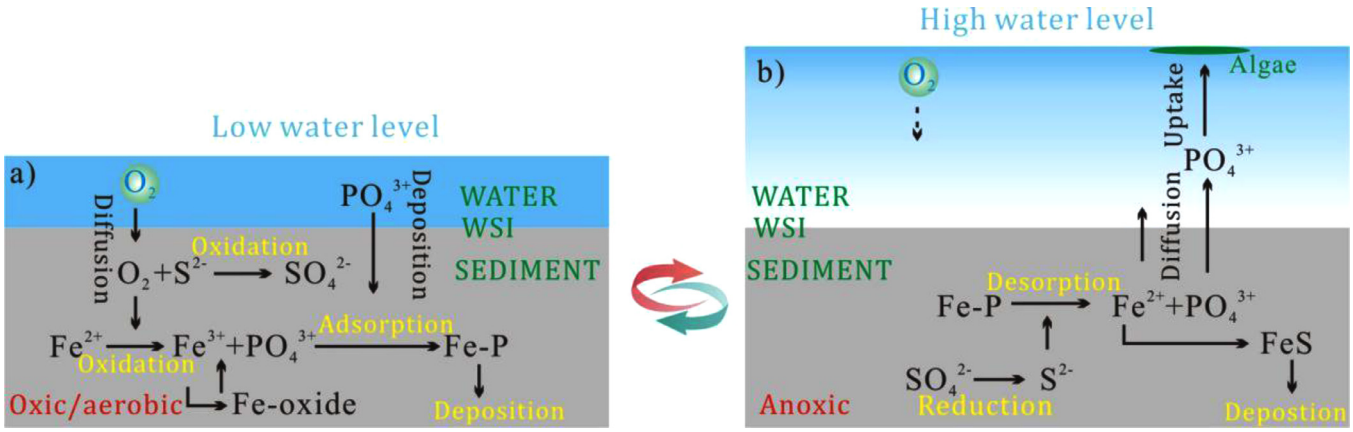

Fig. 9. Schematic of P-Fe-S cycling near the WSI as lake water levels change.

the formation and retention of sulfide in the sediment, and the subsequent acceleration of the desorption of the labile P fraction associated to the Fe(III) (oxy)hydroxides into the aqueous solution under the low DO scenario (Fig. 9).

5. Conclusions

High-resolution *in-situ* fluxes of labile P_{DGT}, $Fe^{2+}{}_{DGT}$, and $S^{2-}{}_{DGT}$ were determined using novel DGT techniques, which displayed significant differences at the water–sediment interface in the various regions of a lake with frequent water-level fluctuations. These analytes in microcosms with low water depth and high DO concentrations obviously decreased after incubation of 30 days, indicating that water–level fluctuation significantly influences adsorption–desorption processes of the P bound to Fe-containing minerals within a short time. Higher labile P_{DGT}, $Fe^{2+}{}_{DGT}$, and $S^{2-}{}_{DGT}$ concentrations were detected at the shallow lake region with more drastic water–depth variations compared with the lake regions with relatively stable water levels. This might be due to the frequent adsorption–desorption of phosphate from the sediment particles to aqueous solution dominated by the variation in oxygen supply. The water–level fluctuations resulted in looser binding on the solid sediment and easier desorption under aerobic conditions, even when the water depth was lower than in other lake regions. Generally speaking, frequent fluctuations of water depth in the lake over time facilitated the formation and retention of sulfide and Fe(II) in the sediment, and the subsequent desorption of the labile P fraction associated to the Fe(III) (oxy)hydroxides into the aqueous solution when the water depth became high. These findings improve insights into the resupply of labile P from Fe-P due to water–level fluctuation in hypereutrophic lakes.

Declaration of Competing Interest

None.

Acknowledgments

This work was funded by National Natural Science Foundation of China (41503099, 31971476), the CAS Interdisciplinary Innovation Team (JCTD-2018-16), and the Key Research Program of Frontier Sciences, CAS (ZDBS-LY-DQC018).

Supplementary materials

Supplementary material associated with this article can be found, in the online version, at doi:10.1016/j.watres.2021.117258.

References

Abreu, P.C., Costa, C.S.B., Bemvenuti, C., Odebrecht, C, Granéli, W., Anesio, A.M., 2006. Eutrophication processes and trophic interactions in a shallow estuary: preliminary results based on stable isotope analysis (δ^{13}C and δ^{15}N). Estuar. Coast. 29, 277–285.

Ahlgren, J., Reitzel, K., Tranvik, L., Gogoll, A., Rydin, E., 2006. Degradation of organic phosphorus compounds in anoxic Baltic Sea sediments: a ^{31}P nuclear magnetic resonance study. Limnol. Oceanogr. 51, 2341–2348.

Ahlgren, J., Tranvik, L., Gogoll, A., Waldebäck, M., Markides, K., Rydin, E., 2005. Sediment depth attenuation of biogenic phosphorus compounds measured by ^{31}P NMR. Environ. Sci. Technol. 39, 867–872.

Alexa, N., Zhang, H., Lead, J.R., 2009. Development of a miniaturized diffusive gradients in thin films (DGT) device. Anal. Chim. Acta 655, 80–85.

Aminot, A., Andrieux, F., 1996. Concept and determination of exchangeable phosphate in aquatic sediments. Wat. Res. 30, 2805–2811.

Anschutz, P., Zhong, S.J., Sundby, B., 1998. Burial efficiency of phosphorus and the geochemistry of iron in continental margin sediments. Limnol. Octwwgr. 43, 53–64.

Azzoni, R., Giordani, G., Bartoli, M., Welsh, D.T, Viaroli, P., 2001. Iron, sulphur and phosphorus cycling in the rhizosphere sediments of a eutrophic *Ruppia cirrhosa* meadow (Valle Smarlacca, Italy). J. Sea Res. 45, 15–26.

Bao, Y.H., Gao, P., He, X.B., 2015. The water-level fluctuation zone of three gorges reservoir-A unique geomorphological unit. Earth-Sci. Rev. 150, 14–24.

Bedrock, C.N., Cheshire, M.V., Chudek, J.A, Fraser, A.R., Goodman, B.A., Shand, C.A., 1995. Effect of pH on precipitation of humic acid from peat and mineral soils on the distribution of phosphorus forms in humic and fulvic acid fractions. Commun. Soil Sci. Plan. 26, 1411–1425.

Borch, T., Masue, Y., ukkadapu, R.K., Fendor, S., 2007. Phosphate imposed limitations on biological reduction and alteration of ferrihydrite. Environ. Sci. Technol. 41, 166–172.

Carpenter, S.R., 2008. Phosphorus control is critical to mitigating eutrophication. PNAS 105, 11039–11040.

Cesbron, F., Metzger, E., Launeau, P., Deflandre, B., Delgard, M.L., de Chanvalon, A.T., Geslin, E., Anschutz, P., Jézéquel, D., 2014. Simultaneous 2D imaging of dissolved iron and reactive phosphorus in sediment porewaters by thin-film and hyperspectral methods. Environ. Sci. Technol. 48, 2282–2816.

Chen, M., Ding, S., Chen, X., Sun, Q., Fan, X., Lin, J., Ren, M., Yang, L., Zhang, C., 2018. Mechanisms driving phosphorus release during algal blooms based on hourly changes in iron and phosphorus concentrations in sediments. Water Res. 133, 153–164.

Chen, M.S., Ding, S.M., Zhang, L.P., Li, Y.Y., Sun, Q., Zhang, C.S., 2017. An investigation of the effects of elevated phosphorus in water on the release of heavy metals in sediments at a high resolution. Sci. Total Environ. 575, 330–337.

Chi, S.Y., Zheng, J.X., Zhao, X.F., Dong, F.Y., Hu, J.X., 2016. Macroinvertebrate communities and the relationships with biotic factors in river-connected lakes in the lower reaches of Yangtze River. China. Environ. Monit. Assess. 188, 577.

Cole, M.L., Valiela, I., Kroeger, K.D., Tomasky, G.L., Cebrian, J., Wigand, C., Richard, A., McKinney, M., Grady, S.P., da Silva, M.H.C., 2004. Assessment of a ^{15}N isotopic method to indicate anthropogenic eutrophication in aquatic ecosystems. J. Environ. Qual. 33, 124–132.

Contreras, S., Werne, J.P., Araneda, A., Urrutia, R., Conejero, C.A., 2018. Organic matter geochemical signatures (TOC, TN, C/N ratio, δ^{13}C and δ^{15}N) of surface sediment from lakes distributed along a climatological gradient on the western side of the southern Andes. Sci. Total Environ. 630, 878–888.

Cosmidis, J., Benzerara, K., Morin, G., Busigny, V., Lebeau, O., Jezequel, D., et al., 2014. Biomineralization of iron-phosphates in the water column of Lake Pavin (Massif Central, France). Geochim. Cosmochim. Ac. 126, 78–96.

Dijkstra, N., Kraal, P., Kuypers, M.M.M., Schnetger, B., Slomp, C.P., 2014. Are Iron-phosphate minerals a sink for phosphorus in anoxic black sea sediments? PLOS ONE 9, e101139.

Ding, S.M., Chen, M., Gong, M.D., Fan, CX., Qin, B.Q., Xu, H., Gao, S.S., Jin, Z.F., Tsang, D.C.W., Zhang, C.S., 2018. Internal phosphorus loading from sediments causes seasonal nitrogen limitation for harmful algal blooms. Sci. Total Environ. 625, 872–884.
Ding, S.M., Han, C., Wang, Y.P., Yao, L., Wang, Y., Xu, D., Sun, Q., Williams, P.N., Zhang, C.S., 2015. In situ, high-resolution imaging of labile phosphorus in sediments of a large eutrophic lake. Water Res 74, 100–109.
Ding, S.M., Xu, D., Bai, X.L., Yao, S.C., Fan, C.X., Zhang, C.S., 2013. Speciation of organic phosphorus in a sediment profifile of Lake Taihu II. Molecular species and their depth attenuation. J. Environ. Sci-China 25, 925–932.
Egger, M., Jilbert, T., Behrends, T., Rivard, C., Slomp, C.P., 2015. Vivianite is a major sink for phosphorus in methanogenic coastal surface sediments. Geochim. Cosmochim. Ac. 169, 217–235.
Egger, M., Kraal, P., Jilbert, T., Sulu-Gambari, F., Sapart, C.J., Röckmann, T., Caroline, P., Slomp, C.P., 2016. Anaerobic oxidation of methane alters sediment records of sulfur, iron and phosphorus in the Black Sea. Biogeosciences 13, 5333–5355.
Gao, J.M, Chen, Z.M., Wang, C., Fang, F., Huang, J.J, Guo, J.S., 2020. Bioavailability of organic phosphorus in the water level fluctuation zone soil and the effects of ultraviolet irradiation on it in the Three Gorges Reservoir. China. Sci. Total Environ. 738, 139912.
Gao, Y.L., Liang, T., Tian, SH., Wang, L.Q., Holm, P.E., Hansen, H.C.B., 2016. High-resolution imaging of labile phosphorus and its relationship with iron redox state in lake sediments. Environ. Pollut. 219, 466–474.
Guan, D.X., Zheng, J.L., Luo, J., Zhang, H., Davison, W., Ma, L.Q., 2017. A diffusive gradients in thin-films technique for the assessment of bisphenols desorption from soils. J. Hazard. Mater. 331, 321–328.
Han, C., Ren, J.H., Wang, Z.D., Tang, H., Xu, D., 2017. A novel hybrid sensor for combined imaging of dissolved oxygen and labile phosphorus flux in sediment and water. Water Res 108, 179–188.
Harper, M.P., Davison, W., Tych, W., 2000. DIFS - a modelling and simulation tool for DGT induced trace metal remobilisation in sediments and soils. Environ. Modell. Softw. 15, 55–66.
Heidari, S., Reyhanitabar, A., Oustan, S., 2017. Kinetics of phosphorus desorption from calcareous soils using DGT technique. Geoderma 305, 275–280.
House, W.A., Denison, F.H., 2000. Factors influencing the measurement of equilibrium phosphate concentrations in river sediments. Wat. Res. 34, 1187–1200.
Jaisi, D.B., Blake., R.E., 2010. Tracing sources and cycling of phosphorus in Peru Margin sediments using oxygen isotopes in authigenic and detrital phosphates. Geochim. Cosmochim. Ac. 74, 3199–3212.
Joshi, S.R., Kukkadapu, R.K., Burdige, D.J., Bowden, M.E., Sparks, D.L., Jaisi, D.P., 2015. Organic matter remineralization predominates phosphorus cycling in the mid-bay sediments in the Chesapeake Bay. Environ. Sci. Technol. 49, 5887–5896.
Kim, L.H., Choi, E., Michael, K., 2003. Sediment characteristics, phosphorus types and phosphorus release rates between river and lake sediments Stenstrom. Chemosphere 50, 53–61.
Kreling, J., Bravidor, J., Engelhardt, C., Hupfer, M., Koschorreck, M., Lorke, A., 2017. The importance of physical transport and oxygen consumption for the development of a metalimnetic oxygen minimum in a lake. Limnol. Oceanogr. 62, 348–363.
Küster-Heins, K., de Lange, G.J., Zabel, M., 2010. Benthic phosphorus and iron budgets for three NW African slope sediments: a balance approach. Biogeosciences 7, 469–480.
Lehto, N.J., Sochaczewski, Ł., Davison, W., Tych, W., Zhang, H., 2008. Quantitative assessment of soil parameter (K-D and Tc) estimation using DGT measurements and the 2D DIFS model. Chemosphere 71, 795–801.
Li, Y.H., Gregory, S., 1974. Diffusion of ions in sea water and in deep-sea sediments. Geochim. Cosmochim. Ac. 88, 703–714.
Li, Z.C., Xu, X.G., Ji, M., Wang, G.X., Han, R.M., Ma, J., Yan, X.C., Liu, J., 2018. Estimating sedimentary organic matter sources by multi-combined proxies for spatial heterogeneity in a large and shallow eutrophic lake. J. Environ. Manage. 147–155.
Li, Z.R., Sheng, Y.Q., Yang, J., Burton, E.D., 2016. Phosphorus release from coastal sediments: Impacts of the oxidation-reduction potential and sulfide. Mar. Poll. Bull. 113, 176–181.
Liu, C., Du, Y.H., Chen, K.N., Ma, S.Z., Chen, B.F., Lan, Y.M., 2019. Contrasting exchanges of nitrogen and phosphorus across the sediment-water interface during the drying and re-inundation of littoral eutrophic sediment. Environ. Pollut. 255, 113356.
Lucotte, M., Mucci, A., Hillaire-marcel, C., Tran, S., 1994. Early diagenetic processes in deep Labrador Sea sediments: reactive and nonreactive iron and phosphorus. Can. J. Earth Sci. 31, 14–27.
Meyers, P.A., 2003. Applications of organic geochemistry to paleolimnological reconstructions: A summary of examples from the Laurentian Great Lakes. Org. Geochem. 34, 261–289.
Monbet, P., Mckelvie, I., Worsfold, A.J., 2008. Combined Gel Probes for the in situ determination of dissolved reactive phosphorus in porewaters and characterization of sediment reactivity. Environ. Sci. Technol. 42, 5112–5117.
Mooney, R.J., Stanley, E.H., Rosenthal, W.C., Esselman, P.C., Kendall, A.D., McIntyre, P.B., 2020. Outsized nutrient contributions from small tributaries to a Great Lake. PNAS 117, 28175–28182.
Murad, E., Cashion, J., 2004. Mossbauer Spectroscopy of Environmental Materials and Their Industrial Utilization. Kluwer Academic Publishers, Norwell, Massachusetts, USA.
Naylor, C., Davison, W., Motelica-Heino, M., Van Den Berg, G.A., Van Der Heijdt, L.M., 2004. Simultaneous release of sulfide with Fe, Mn, Ni and Zn in marine harbour sediment measured using a combined metal/sulfide DGT probe. Sci. Total Environ. 328, 275–286.
Norgbey, E., Li, Y.P., Ya, Z., Li, R.H., Nwankwegu, A.S., Takyi-Annan, G.E., Luo, F., Jin, W., Huang, Y.N., Sarpon, L., 2020. High resolution evidence of iron-phosphorus-sulfur mobility at hypoxic sediment water interface: An insight to phosphorus remobilization using DGT-induced fluxes in sediments model. Sci. Total Environ. 724, 138204.
Nriagu, J.O., Dell, C.I., 1974. Diagenetic formation of lron phosphates in recent lake sediments. Am. Mineral. 59, 934–946.
O'Connell, D.W., Jensen, M.M., Jakobsen, R., Thamdrup, B., Andersen, T.J., Kovacs, A., Hansen, H.C.R., 2015. Vivianite formation and its role in phosphorus retention in Lake Ørn, Denmark. Chem. Geol. 409, 42–53.
Olila, O.G., Reddy, K.R., 1997. Influence of redox potential on phosphate-uptake by sediments in two sub-tropical eutrophic lakes. Hydrobiologia 345, 45–57.
Pant, H.K., Reddy, K.R., Dierberg, F.E., 2002. Bioavailability of organic phosphorus in a submerged aquatic vegetation–dominated treatment wetland. J. Environ. Qual. 31, 1748–1756.
Price, H.L., Teasdale, P.R., Jolley, D.F., 2013. An evaluation of ferrihydrite- and Metsorb ™ -DGT techniques for measuring oxyanion species (As, Se, V, P): Effective capacity, competition and diffusion coefficients. Anal. Chim. Acta 803, 56–65.
Qin, B.Q., Zhou, J., Elser, J.J., Gardner, W.S., Deng, J.M., Brookes, J.D., 2020. Water depth underpins the relative roles and fates of nitrogen and phosphorus in lakes. Environ. Sci. Technol. 54, 3191–3198.
Quinlan, R., Filazzola, A., Mahdiyan, O., Shuvo, A., Blagrave, K., Ewins, C., Moslenko, L., Gray, D.K., O'Reilly, C.M., Sharma, S., 2021. Relationships of total phosphorus and chlorophyll in lakes worldwide. Limnol. Oceanogr. 66, 392–404.
Reitzel, K., Ahlgren, J., Gogoll, A., Jensen, H.S., Rydin, E., 2006. Characterization of phosphorus in sequential extracts from lake sediments using ^{31}P nuclear magnetic resonance spectroscopy. Can. J. Fish. Aquat. Sci. 63, 1686–1699.
Riber, H.H., Wetzel, R.G., 1987. Boundary-layer and internal diffusion effects on phosphorus fluxes in Lake Periphyton. Limnol. Oceanogr. 32, 1181–1194.
Rozan, T.F., Taillefert, M., Trouwborst, R.E., Glazer, B.T., Ma, S.F., Herszage, J., Valdes, L.M., Price, K.S., Luther III, G.W., 2002. Iron-sulfur-phosphorus cycling in the sediments of a shallow coastal bay: implications for sediment nutrient release and benthic macroalgal blooms. Limnol. Oceanogr. 47, 1346–1354.
Ruban, D., Brigault, S., Demare, D., Philippe, A.M., 1999. An investigation of the origin and mobility of phosphorus in freshwater sediments from Bort-Les-Orgues Reservoir, France. J Environ Monit 1, 403–407.
Ruban, V., López-Sánchez, J.F., Pardo, P., Rauret, G., Muntau, H., Quevauviller, P., 2001. Harmonized protocol and certified reference material for the determination of extractable contents of phosphorus in freshwater sediments-A synthesis of recent works. Fresenius J. Anal. Chem. 370, 224–228.
Ruttenberg, K.C., Berner, R.A., 1993. Authigenic apatite formation and burial in sediments from non-upwelling, continental margin environments. Geochim. Cosmochim. Ac. 57, 991–1007.
Rydin, E., 2000. Potentially mobile phosphorus in Lake Erken sediment. Water Res. 34, 2037–2042.
Shinohara, R., Imai, A., Kawasaki, N., Komatsu, K., Kohzu, A., Miura, S., Sano, T., Satou, T., Tomioka, N., 2012. Biogenic phosphorus compounds in sediment and suspended particles in a shallow eutrophic lake: a ^{31}P–nuclear magnetic resonance (^{31}P NMR) study. Environ. Sci. Technol. 46, 10572–10578.
Simpson, Z.P., McDowell, R.W., Condron, L.M., 2019. The error in stream sediment phosphorus fractionation and sorption properties effected by drying pretreatments. J. Soil. Sediment. 19, 1587–1597.
Stockdale, A., Davison, W., Zhang, H., 2009. Micro-scale biogeochemical heterogeneity in sediments: a review of available technology and observed evidence. Earth-Sci. Rev. 92, 81–97.
Sochaczewski, Ł., Tych, W., Davison, B., Zhang, H., 2007. 2D DGT induced fluxes in sediments and soils (2D DIFS). Environ. Modell. Softw. 22, 14–23.
Sun, Q.Y., Sheng, Y.Q., Yang, J., Bonito, M.D., Mortimer, R.J.G., 2016. Dynamic characteristics of sulfur, iron and phosphorus in coastal polluted sediments, north China. Environ. Pollut. 219, 588–595.
Ullman, W.J., Aller, R.C., 1982. Diffusion coefficients in nearshore marine sediments. Limnol. Oceanorg. 27, 552–556.
Vollenweider, R.A., 1975. Input-output models with special reference to the phosphorus loading concept in limnology. Schweiz. Z. Hydrol. 37, 53–74.
Wang, C., Fang, F., Yuan, Z., Zhang, R., Zhang, W., Guo, J., 2020. Spatial variations of soil phosphorus forms and the risks of phosphorus release in the water-level fluctuation zone in a tributary of the Three Gorges Reservoir. Sci. Total Environ. 699, 134124.
Wu, S.J., Zhao, Y.P., Chen, Y.Y., Dong, X.M., Wang, M.Y., Wang, G.X., 2019. Sulfur cycling in freshwater sediments: a cryptic driving force of iron deposition and phosphorus mobilization. Sci. Total Environ. 657, 1294–1303.
Wu, Z.H., Wang, S.R., Zhang, L., Jiao, L.X., 2016. DGT induced fluxes in sediments model for the simulation of phosphorus process and the assessment of phosphorus release risk. Environ. Sci. Pollut. Res. 23, 14608–14620.
Xia, S.P., Song, Z.L., Li, Q., Guo, L.D., Yu, C.X., Singh, B.P., Fu, X.L., Chen, C.M., Wang, Y.D., Wang, H.L., 2021. Distribution, sources, and decomposition of soil organic matter along a salinity gradient in estuarine wetlands characterized by C:N ratio, δ^{13}C-δ^{15}N, and lignin biomarker. Global Change Biol 27, 417–434.
Xu, D., Chen, Y., Ding, S., Sun, Q., Wang, Y., Zhang, C., 2013. Diffusive gradients in thin films technique equipped with a mixed binding gel for simultaneous measurements of dissolved reactive phosphorus and dissolved iron. Environ. Sci. Technol. 47, 10477–10484.

Xu, D., Wu, W., Ding, S.M., Sun, Q., Zhang, C.S, 2012. A high-resolution dialysis technique for rapid determination of dissolved reactive phosphate and ferrous iron in pore water of sediments. Sci. Total Environ. 421-422, 245–252.
Yuan, H.Z., Li, Q., Kukkadapu, R.K., Liu, E.F., Yu, J.H., Fang, H., Li, H., Jaisi, D.B., 2019. Identifying sources and cycling of phosphorus in the sediment of a shallow freshwater lake in China using phosphate oxygen isotopes. Sci. Total Environ. 676, 823–833.
Yuan, H.Z., Tai, Z.Q., Li, Q., Zhang, F.M., 2020c. Characterization and source identification of organic phosphorus in sediments of a hypereutrophic lake. Environ. Pollut. 257, 113500.
Zhao, Y.P., Zhang, Z.Q., Wang, G.X., Li, X.J., Ma, J., Chen, S., Deng, H., Annalisa, O.H., 2019. High sulfide production induced by algae decomposition and its potential stimulation to phosphorus mobility in sediment. Sci. Total Environ. 650, 163–172.